Research Article | Vol. 32, No. 5 / 26 Feb 2024 / Optics Express 8415

Optics EXPRESS

Linearized EUV mask optimization based on the adjoint method

PINXUAN HE,[1] JIAMIN LIU,[1,3] HONGGANG GU,[1] HAO JIANG,[1] AND SHIYUAN LIU[1,2,4]

[1] State Key Laboratory of Intelligent Manufacturing Equipment and Technology, Huazhong University of Science and Technology, Wuhan, Hubei 430074, China
[2] Optics Valley Laboratory, Wuhan, Hubei 430074, China
[3] jiaminliu@hust.edu.cn
[4] shyliu@hust.edu.cn

Abstract: Mask optimization, a compensation method for the thick mask effect and the optical proximity effect in projection lithography, is essential for advanced EUV-enabled production nodes. However, owing to high computation costs and the absence of gradient calculations, it is challenging to optimize EUV masks under rigorous consideration of the thick mask effect. In this work, a linearized EUV mask optimization method based on the adjoint method is proposed to provide fast and effective optimizations. The adjoint method is introduced to calculate the gradient of the EUV mask model. Additionally, a linearized gradient is proposed to quickly compensate for wafer pattern distortion caused by the prominent thick mask effect. Two examples of the EUV mask optimization implemented with a two-step strategy were provided, from which it was observed that the linearized gradient can improve the efficiency by about 40% in the coarse optimization step. The proposed method is promising for accurate full-chip EUV mask optimization.

© 2024 Optica Publishing Group under the terms of the Optica Open Access Publishing Agreement

1. Introduction

For decades, projection lithography has pursued higher resolution by various methods [1], including alternating phase shifting mask [2], off-axis illumination [3], and multiple patterning [4]. Among these methods, mask optimization (MO) [5] is one of the most promising methods to explore the limits of lithography and has been widely used in deep ultraviolet lithography (DUVL) [6–8]. As the successor of the DUVL, extreme ultraviolet lithography (EUVL) bears not solely the optical proximity effect but also the severe thick mask effect [9], which makes the MO an indispensable tool to extend the lifespan of Moore's law [10].

The MO has been studied extensively since its first commercialization in the 2000s [11,12], which can be classified into the end-to-end and iterative MO. The former [13–16] trains neural networks with thousands of reference datasets obtained from the iterative MO, after which optimized mask patterns can be predicted directly. The end-to-end MO is fast, while it cannot guarantee obtaining a local optimal solution and usually is used to generate initial patterns for the iterative MO [17]. The iterative MO simulates the lithography process using the mask model, projection lens model and resist model to get wafer patterns, then iteratively optimizes mask patterns based on the simulation results until wafer patterns meet requirements. According to optimization algorithm, the iterative MO can be divided into the heuristic- and gradient-based MO. Although the heuristic-based MO does not need the gradient, it is typically slower than the gradient-based MO [18–20]. Therefore, the gradient-based MO is used most frequently and it is essential to calculate the gradient for reducing the runtime of the MO.

The difficulty of gradient calculations mainly depends on the thick mask model, while the derivations of other components of the lithography model like the projection lens model and resist model are well-established [21,22]. Ma et al. proposed a gradient calculation for boundary

#517783 https://doi.org/10.1364/OE.517783
Journal © 2024 Received 8 Jan 2024; revised 9 Feb 2024; accepted 10 Feb 2024; published 22 Feb 2024

layer model [23] in the DUVL. However, the mask model is inapplicable for the EUV mask with the severe thick mask effect. Considering that the application of curvilinear patterns is inevitable with the emerging of multi-beam mask writing (MBMW) [24,25], it is also necessary for the mask model to be compatible with complex curvilinear patterns. To meet the requirements, a fast mask model based on modified Born series (MBS) [26] was proposed in our previous paper. However, there is a lack of gradient calculation methods corresponding to this mask model for the highly efficient MO.

Adjoint method is widely applied for optical inverse design [27,28]. With only two electromagnetic simulations, one can calculate the gradient of an objective function with respect to all design variables in the simulation domain [29]. In this work, the adjoint method is introduced to the gradient calculation of the EUV thick mask model for the first time. With rigorous consideration of the thick mask effect, the mask can be optimized iteratively based on the gradient. Compared to the DUVL, there are more differences between wafer patterns and mask patterns in the EUVL because of the more significant thick mask effect. Therefore, EUV masks need more optimization. To reduce the computational cost of the EUV mask optimization, a linearized gradient, which ignores resist models in the gradient calculation, is proposed. A detail of the gradient calculation is presented in Section 2. The effectiveness and superiority of the proposed method are demonstrated with two examples of the EUV mask optimization implemented in a two-step strategy in Section 3.

2. Theory and methods

2.1. Mask optimization

The MO is treated as a minimization problem, in which the mask pattern is the design variable and the normalized wafer pattern fidelity is the cost function. The mask pattern is represented by $\mathbf{\Theta} \in \mathbb{R}^{M\times N}$. The cost function is defined as the normalized square of the Euler distance between the wafer pattern and target pattern, which implies the average edge placement error along the target contour.

$$F(\mathbf{\Theta}) = \frac{\left\|\mathbf{w}^{\mathrm{c}}(\mathbf{\Theta}) - \mathbf{w}^{\mathrm{t}}\right\|_2^2}{C} \tag{1}$$

where $\mathbf{w}^{\mathrm{c}}$ is the wafer pattern of the corresponding mask pattern $\mathbf{m}$ calculated by lithography models; $\mathbf{w}^{t}$ is the target pattern; The notation $\|\cdot\|_2^2$ represents the square of l_2-norm; C is the perimeter of the target pattern. The mask optimization problem can be express as

$$\hat{\mathbf{\Theta}} = \arg\min_{\mathbf{\Theta}} F(\mathbf{\Theta}) \tag{2}$$

With the aim of high performance and manufacturability, a two-step optimization strategy is applied, which is shown in Fig. 1. In the coarse optimization step, the continuous mask is optimized with the linearized gradient, until the normalized cost function is smaller than 1 or the iteration number exceeded 60. Then, the obtained mask pattern is binarized and filtered. In the fine optimization step, the binary mask pattern is represented by the level set method [30] and optimized with the normal gradient. A fixed number of iterations are conducted to find the minimum of the cost function in this step. There is a similar strategy that uses an aerial image penalty term as the cost function in the coarse step [31]. Note this work applies different gradients instead of different cost functions between the two steps, while the substitution of the cost function might lead to ineffective optimization.

The optimized patterns might contain small undesired artifacts, such as isolated voids, protrusions, and irregular edges, which can result in poor manufacturability [21,32–33]. These artifacts can be taken as noise and removed by filtering operation between the two steps [34]. During the level set evolution, an extra motion, driven by the mean curvature of the pattern

Optics EXPRESS

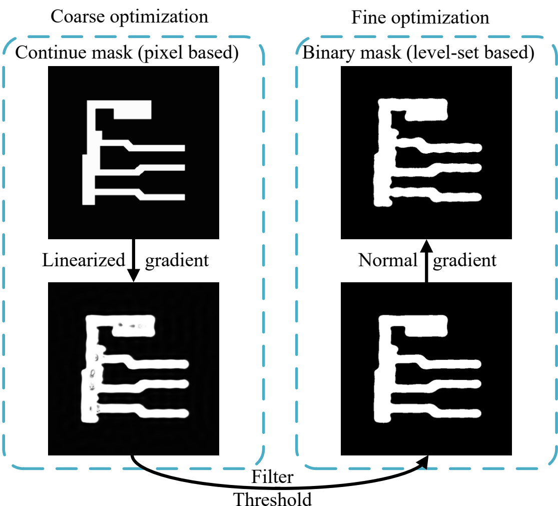

Fig. 1. A two-step optimization strategy. In the coarse optimization step, the continuous mask is optimized with the linearized gradient. Then, the obtained mask pattern is filtered and binarized to improve the manufacturability. In the fine optimization step, the binary mask pattern is represented by the level set method and optimized with the normal gradient.

contour [30], is applied, which can contribute to meeting the curvature requirements of the mask manufacturing rules checking (MRC) and prohibit the emergence of small features. To some extent, these methods can enhance the manufacturability.

2.2. Rigorous EUVL model

A lithography simulation model usually consists of a mask model, a vector projection lens model, and a resist model. Considering the complex thick mask effect, a mask model based on the MBS is adopted, which significantly outperforms the FDTD in terms of speed while maintaining comparable accuracy [26,35]. The mask model can be represented as

$$\mathbf{E}^{\mathrm{mask}} = \mathbf{GV}(\boldsymbol{\Theta})\mathbf{E}^{\mathrm{mask}} + \mathbf{GS} \tag{3}$$

where $\mathbf{E}^{\mathrm{mask}}$ is a vector containing the field at all points in the simulation domain; $\mathbf{G}$ is a matrix representing the convolution; $\mathbf{V}$ is a diagonal matrix containing the scattering potential which is determined by the mask pattern $\mathbf{m}$; $\mathbf{S}$ is a vector representing the incident field from a single source points in the partially coherent illumination. The derivation is based on coherent illumination for simplicity. After solving the MBS with the fix-point iteration, the mask near field $\mathbf{E}^{\mathrm{near}}$ can be extracted from $\mathbf{E}^{\mathrm{mask}}$ and propagated to the wafer plane with the vector projection lens model.

$$\begin{bmatrix} \mathbf{E}_{\mathrm{x}}^{\mathrm{wafer}} \\ \mathbf{E}_{\mathrm{y}}^{\mathrm{wafer}} \\ \mathbf{E}_{\mathrm{z}}^{\mathrm{wafer}} \end{bmatrix} = \mathbf{H} \begin{bmatrix} \mathbf{E}_{\mathrm{x}}^{\mathrm{near}} \\ \mathbf{E}_{\mathrm{y}}^{\mathrm{near}} \\ \mathbf{E}_{\mathrm{z}}^{\mathrm{near}} \end{bmatrix} \tag{4}$$

where the vector projection operator $\mathbf{H}$ represents the propagation of the field from the mask plane to the wafer plane. A detailed description of $\mathbf{H}$ can be found in Ref. [36]. Then, the aerial image, the distribution of intensity, is obtained by summing the intensity of all three components

Optics EXPRESS

of $\mathbf{E}^{\mathrm{wafer}}$.

$$\mathbf{I} = \left|\mathbf{E}_{\mathrm{x}}^{\mathrm{wafer}}\right|^{2} + \left|\mathbf{E}_{\mathrm{y}}^{\mathrm{wafer}}\right|^{2} + \left|\mathbf{E}_{\mathrm{z}}^{\mathrm{wafer}}\right|^{2} \tag{5}$$

The feature of resists is the nonlinear response to the intensity [37], which is usually approximated by a sigmoid function. The wafer pattern can be obtained from the aerial image.

$$\mathbf{w}^{\mathrm{c}} = sig\left(\mathbf{I}\right) = \frac{1}{1 + \exp\left[-a\left(\mathbf{I} - t_{\mathrm{r}}\right)\right]} \tag{6}$$

where a and t_{r} represent the steepness and threshold of the resist model, respectively. Note that the proposed method imposes no restrictions on the resist model except for the requirement of differentiability.

2.3. Gradient calculation

The primary challenge in gradient calculations of the rigorous EUVL model lies with the EUV mask model. To solve this problem, the adjoint method is introduced for the first time. The gradient of the cost function can be expressed as

$$\frac{\partial F}{\partial \mathbf{\Theta}} = \mathrm{Re}\left\{\mathbf{E}^{A}\hat{\mathbf{E}}^{\mathrm{mask}}\mathbf{C}_{\mathrm{v}}\right\} \tag{7}$$

where $\hat{\mathbf{E}}^{\mathrm{mask}} = diag(\mathbf{E}^{\mathrm{mask}})$; $\mathbf{E}^{A}$ is the result of adjoint simulations; $\mathbf{C}_{\mathrm{v}}$ is a diagonal matrix representing the partial derivative of $\mathbf{V}$ with respect to $\mathbf{\Theta}$. The detailed derivation of the gradient calculation and $\mathbf{C}_{\mathrm{v}}$ can be found in Supplement 1. The adjoint simulations are identical to the forward simulations in Eq. (3), except for the sourece term, which implies that the implementation and the computational load are the same too. Based on the gradient, the mask can be optimized efficiently.

Different from the DUV MO, there are much more modifications needed in the EUV MO due to the more prominent thick mask effect. Besides, it is found that the modification of the mask pattern for each iteration mainly occurs at the edge of previous patterns. Many iterations with heavy computational costs are needed to obtain satisfactory mask patterns, which can be attributed to the nonlinear response of the resist. At the region with the intensity away from the threshold of the resist, a small perturbation in the intensity cannot induce a discernible change on the wafer pattern. Therefore, the gradient away from the edge of the mask pattern is nearly zero. Another reason for the inefficient modification is that the definition of the gradient is based on the assumption of linearity. However, the cost function is inconsistent with the assumption because of the nonlinear response of resists.

To solve this contradiction and accelerate the optimization, the linearized gradient is proposed. The partial derivative of the cost function F with respect to the intensity $\mathbf{I}$ is

$$\frac{\partial F}{\partial \mathbf{I}} = \frac{\partial F}{\partial \mathbf{w}^{\mathrm{c}}}\frac{\partial \mathbf{w}^{\mathrm{c}}}{\partial \mathbf{I}} \tag{8}$$

Then, the linearized gradient can be obtained by ignoring the resist model.

$$\frac{\partial F}{\partial \mathbf{I}} = \frac{\partial F}{\partial \mathbf{w}^{\mathrm{c}}} \tag{9}$$

The linearized gradient allows pattern modification anywhere, rather than being confined solely to the edge of previous patterns. Note that the linearized gradient is not as accurate as the normal gradient, but it is more effective than the latter. Two examples are provided in Section 3. to show the superiority of the linearized gradient.

3. Results and discussion

The proposed method can be applied to various situations. It is necessary to clarify the model and optimization parameters. The wavelength was 13.5 nm. The s-polarized light hit the mask at an incident angle of 6°. The binary dark-field EUV mask consisted of the absorber and multilayer [38]. The absorber material was TaN with the refractive index N = 0.9385 + 0.03776i. The absorber thickness was 50 nm. The multilayer stack parameters from Ref. [39] were adopted. Note that the proposed method is also applicable to the attenuated phase-shift mask with standard multilayer blanks [40]. For the projection lens model, the demagnification factor and numerical aperture (NA) were 4 and 0.33, respectively. The aberration term was ignored. The steepness a and threshold t_r in the resist model were 80 and 0.4, respectively. The resist model was used in the lithography simulations and the calculation of the normal gradient, while it would be ignored in the calculation of the linearized gradient. Equation (2) was solved by the steepest descent method iteratively. The initial step size s for the first iteration was $0.75\pi/\max(\partial F/\partial \boldsymbol{\Theta})$, while s for other iterations was the optimized step size of previous iterations. The actual step sizes were obtained by the Brent's method [41] with an evaluation number of 5 and a maximum step size of $2s$. The filter used was a Gaussian filter with a standard deviation of 6. The strength factor of the curvature motion in the level set evolution is 0.008.

All the computations were performed on a virtual machine based on the Intel Xeon Gold 6230R architecture, with 8 allocated cores and 32 GiB of memory. Besides, one NVIDIA Tesla V100S with 32 GiB of memory was used. The calculations were implemented using MATLAB. The maximum GPU memory usage was approximately 7.5 GiB during the MO.

3.1. Gradient verification

Before optimizing the EUV masks, it is necessary to verify the accuracy of gradient calculations. The reference gradient was obtained from a simple first-order difference.

$$\frac{\partial F(\boldsymbol{\Theta})}{\partial \boldsymbol{\Theta}_j} = \frac{F\left(\boldsymbol{\Theta} + d\boldsymbol{\Theta}_j\right) - F(\boldsymbol{\Theta})}{d\boldsymbol{\Theta}_j}, j = 1, \ldots, MN \tag{10}$$

where $d\boldsymbol{\Theta}_j$ represents a perturbation in the j-th design variable. The accuracy of the difference equation depends on the size of the perturbation which is necessary to maintain a balance between the approximation and rounding errors [42]. Therefore, the gradients with perturbations of different sizes were calculated to provide solid references. The distribution of the variable $\boldsymbol{\Theta}$ and target pattern are shown in Fig. 2. The test points locate at a line segment with y = 0 nm and x = [-200, 300]. The gradients are normalized and shown in Fig. 2(c). The great consistency between the three reference gradients and that from adjoint simulation can be observed, which demonstrates the accuracy of gradient calculations.

3.2. Mask optimization examples

Two examples of the EUV thick mask optimization are presented in this section. The target patterns, including a logic pattern and a BigMaC [43] pattern, are discretized into 664×672 and 700×632 pixels, respectively. The pixel size is 3.375 nm. The results are shown in Fig. 3 and Fig. 4. The minimum dimensions of both the patterns are 20 nm on wafer scale. The upper-left figure shows the original and optimized patterns in green and blue, respectively. The corresponding wafer patterns, compared with the target pattern in red, are shown in the right figure. The figures below are the corresponding zoomed-in views.

Due to the mask shadow effect [9], the original wafer patterns shrink compared to the target patterns. To compensate for the shrinkage, the openings of the mask patterns are enlarged, which provides excellent contour fidelity in both examples. The aerial and resist images are provided in Supplement 1. Compared to the logic pattern, the smaller interval between the features in the

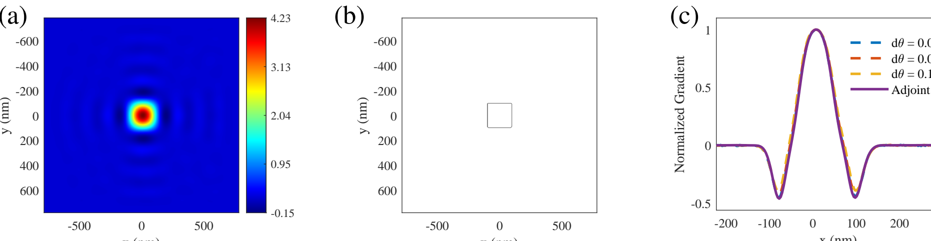

Fig. 2. An example for verification of the gradient calculation. (a) The distribution of design variable $\mathbf{\Theta}$. (b) The target wafer pattern. (c) Comparison between the reference gradients with perturbations of different sizes and that from the adjoint simulation at a line segment with y = 0 nm and x = [-200, 300] nm.

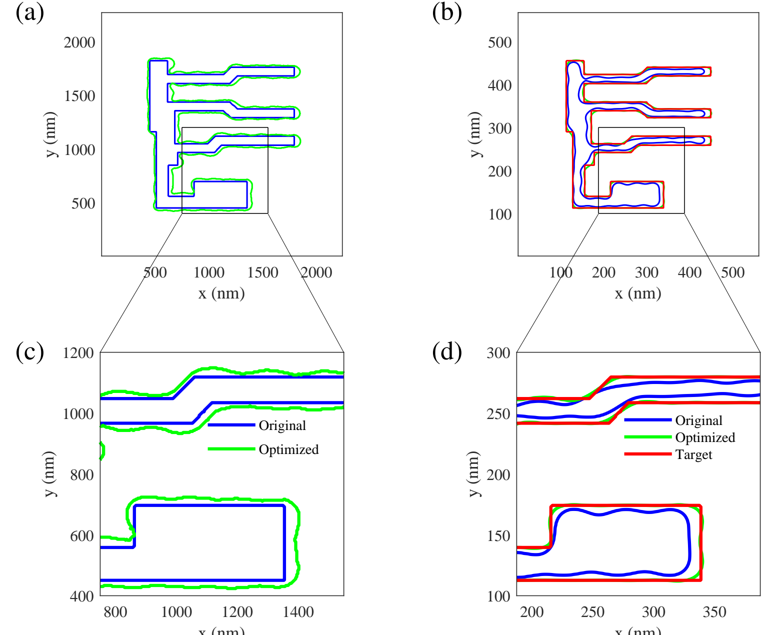

Fig. 3. The mask optimization for the logic pattern with the minimum dimension of 20 nm on wafer scale. (a) The original and optimized mask pattern. (b) The corresponding wafer pattern. The figures below are the corresponding zoomed-in views.

BigMaC pattern would lead to stronger interaction. Therefore, it is more challenging to optimize the BigMaC pattern. For the logic and BigMaC pattern, the cost functions of the optimized patterns are 90% and 86% smaller than those of the original patterns, respectively.

The convergence of the cost function with the linearized and normal gradient is shown in Fig. 5. For the case of the normal gradient, the normal gradient was used in both two steps. There are some turning points at the normalized cost of 1, at which the mask patterns are binarized and filtered to reduce the complexity. With the linearized gradient, the numbers of iterations required to reach the turning points are decreased by about 44% and 57% for the logic and BigMaC pattern, respectively, which demonstrates the superiority of the linearized gradient.

The runtime of the mask optimizations is shown in Table 1. The forward simulations of EUV masks are accelerated by the initial condition from the field of the mask with the last pattern

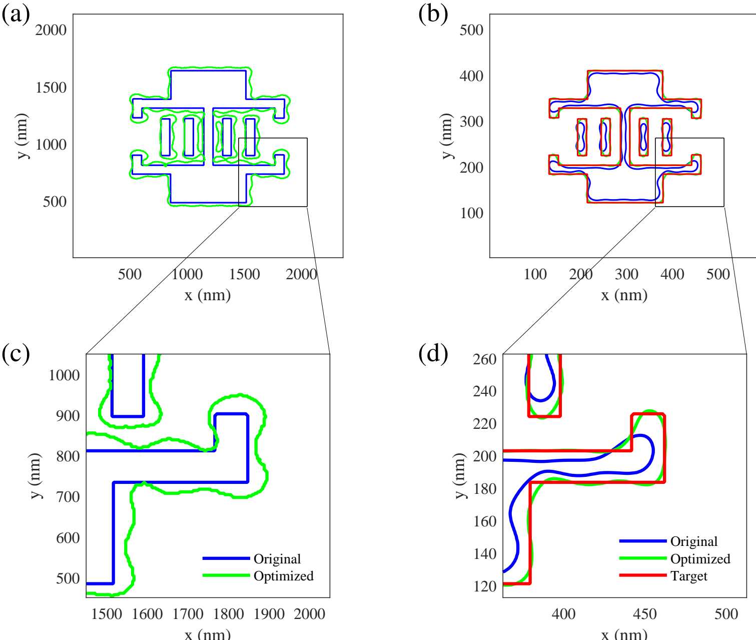

Fig. 4. The mask optimization for the BigMaC pattern with the minimum dimension of 20 nm on wafer scale. (a) The original and optimized mask pattern. (b) The corresponding wafer pattern. The figures below are the corresponding zoomed-in views.

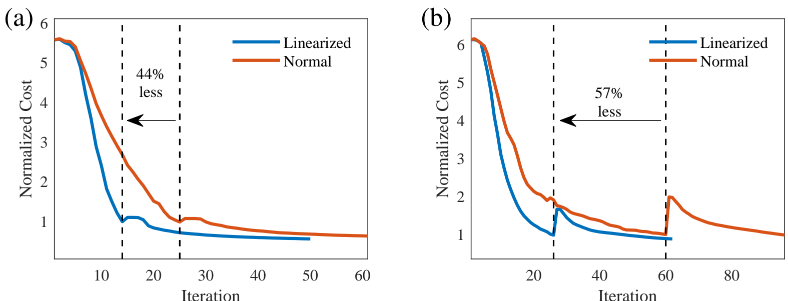

Fig. 5. Convergence of normalized cost function with linearized and normal gradient for (a) the logic and (b) the BigMaC pattern. The optimization adopts the two steps strategy. In the coarse step, the iteration stops when the normalized cost is smaller than 1. Then, the obtained masks are binarized and filtered, which leads to the turning points of the cost function. The filtered masks are optimized for 36 iterations in the fine step to get the optimized masks.

(PatternACC) [26]. In other words, the greater the similarity between the patterns, the less time needed. Given the linearized gradient tends to introduce more modifications than the normal one, the reduction in time, which is 42% and 47% respectively, is slightly less pronounced than the reduction in iteration number. Due to the step size search, the forward simulation has been executed five times more frequently than the adjoint simulation. Then, the estimated average effect of the PatternACC with the linearized gradient is about 48%. The average runtime with the linearized gradient is about 400 seconds.

The mask optimizations in this work are conducted under a single source point. The proposed method can be extended to the partially coherent illumination with the Abbe integration [44].

Optics EXPRESS

Table 1. Runtime of the mask model and MO. The data are presented in seconds.

Pattern		Logic		BigMac	
Method		Linearized	Normal	Linearized	Normal
Step 1	Forward	74	127	91	160
	Adjoint	25	45	31	72
Step 2	Forward	158	178	93	92
	Adjoint	64	65	43	43
Mask Model		322	416	258	367
Mask Optimization		421	526	385	513

However, the PatternACC may be unsuitable for the partially coherent illumination due to the difficulty of handling vast amounts of data. Assuming that the runtime of the MO is linear to the number of source points N_{p}, the runtime is estimated as $400 \times 2 \times N_{\mathrm{p}}$ seconds. For example, the runtime of the MO with 108 source points is 1 day. Further investigation about the selection of the source points and speed improvement, is required for a reliable and pratical MO under the partially coherent illumination. Given that the current NA is 0.33, the runtime can be reduced by replacing the vector model with a scalar one, while additional research about the impact on accuracy is required. The vector model used in this work can be applied to situations with high NA.

4. Conclusion

In summary, a linearized EUV mask optimization based on the adjoint method is proposed. The adjoint method is first introduced into gradient calculations of the EUV thick mask model, which makes the gradient-based rigorous EUV MO possible. Moreover, the linearized gradient is proposed to reduce the iterations of the optimization. It was shown that the linearized gradient was more efficient than the normal one in the coarse optimization step, and half of the iterations can be saved. This work contributes a solid foundation for the further development of EUV computational lithography, and future studies can explore its application on partially coherent illumination with acceptable runtime.

Funding. National Natural Science Foundation of China (52130504, 52305577); Key Research and Development Plan of Hubei Province (2021BAA013, 2022BAA013); Major Program (JD) of Hubei Province (2023BAA008-2); Innovation Project of Optics Valley Laboratory (OVL2023PY003); Nationally Funded Postdoctoral Fellow Research Program (GZB20230244).

Acknowledgments. The authors are grateful for the technical support from the Experiment Centre for Advanced Manufacturing and Technology in School of Mechanical Science and Engineering of HUST. The computation was completed on the HPC Platform of Huazhong University of Science and Technology.

Disclosures. The authors declare no conflicts of interest.

Data availability. The data underlying the results presented in this paper are not publicly available at this time but may be obtained from the authors upon reasonable request.

Supplemental document. See Supplement 1 for supporting content.

References

1. T. Cecil, D. Peng, D. Abrams, *et al.*, "Advances in inverse lithography," ACS Photonics **10**(8), 910–918 (2023).
2. L. W. Liebmann, I. C. Graur, W. C. Leipold, *et al.*, "Alternating phase-shifted mask for logic gate levels, design, and mask manufacturing," in *Optical Microlithography XII*, vol. 3679 L. V. den Hove, ed., International Society for Optics and Photonics (SPIE, 1999), pp. 27–37.
3. C. A. Mack, "Optimum stepper performance through image manipulation," SPIE milestone series **178**, 614–620 (2004).

Optics EXPRESS

4. D. Z. Pan, L. Liebmann, B. Yu, *et al.*, "Pushing multiple patterning in sub-10nm: Are we ready?" in *Proceedings of the 52nd Annual Design Automation Conference*, (Association for Computing Machinery, New York, NY, USA, 2015), DAC '15.
5. L. Pang, "Inverse lithography technology: 30 years from concept to practical, full-chip reality," J. Micro/Nanopattern. Mats. Metro. **20**(03), 030901 (2021).
6. V. Singh, B. Hu, K. Toh, *et al.*, "Making a trillion pixels dance," in *Optical Microlithography XXI*, vol. 6924 H. J. Levinson and M. V. Dusa, eds., International Society for Optics and Photonics (SPIE, 2008), p. 69240S.
7. L. Pang, E. V. Russell, B. Baggenstoss, *et al.*, "Study of mask and wafer co-design that utilizes a new extreme SIMD approach to computing in memory manufacturing: full-chip curvilinear ILT in a day," in *Photomask Technology 2019*, vol. 11148 J. H. Rankin and M. E. Preil, eds., International Society for Optics and Photonics (SPIE, 2019), p. 111480U.
8. L. Pang, G. Dai, T. Cecil, *et al.*, "Validation of inverse lithography technology (ILT) and its adaptive SRAF at advanced technology nodes," in *Optical Microlithography XXI*, vol. 6924 H. J. Levinson and M. V. Dusa, eds., International Society for Optics and Photonics (SPIE, 2008), p. 69240T.
9. A. Erdmann, D. Xu, P. Evanschitzky, *et al.*, "Characterization and mitigation of 3d mask effects in extreme ultraviolet lithography," Adv. Opt. Technol. **6**(3-4), 187–201 (2017).
10. K. Braam, K. Selinidis, W. Hoppe, *et al.*, "EUV mask synthesis with rigorous ILT for process window improvement," in *Design-Process-Technology Co-optimization for Manufacturability XIII*, vol. 10962 J. P. Cain, ed., International Society for Optics and Photonics (SPIE, 2019), p. 109620P.
11. Y. Liu, D. Abrams, L. Pang, *et al.*, "Inverse lithography technology principles in practice: unintuitive patterns," in *25th Annual BACUS Symposium on Photomask Technology*, vol. 5992 J. T. Weed and P. M. Martin, eds., International Society for Optics and Photonics (SPIE, 2005), p. 599231.
12. L. Pang, N. Shamma, P. Rissman, *et al.*, "Laser and e-beam mask-to-silicon with inverse lithography technology," in *25th Annual BACUS Symposium on Photomask Technology*, vol. 5992 J. T. Weed and P. M. Martin, eds., International Society for Optics and Photonics (SPIE, 2005), p. 599221.
13. B. Jiang, L. Liu, Y. Ma, *et al.*, "Neural-ilt: Migrating ilt to neural networks for mask printability and complexity co-optimization," in *Proceedings of the 39th International Conference on Computer-Aided Design*, (Association for Computing Machinery, New York, NY, USA, 2020), ICCAD '20.
14. J.-T. Chen, Y.-Y. Zhao, Y. Zhang, *et al.*, "Label-free neural networks-based inverse lithography technology," Opt. Express **30**(25), 45312–45326 (2022).
15. B. Jiang, X. Zhang, L. Liu, *et al.*, "Building up end-to-end mask optimization framework with self-training," in *Proceedings of the 2021 International Symposium on Physical Design*, (Association for Computing Machinery, New York, NY, USA, 2021), ISPD '21, p. 63–70.
16. T. Cecil, K. Braam, A. Omran, *et al.*, "Establishing fast, practical, full-chip ILT flows using machine learning," in *Optical Microlithography XXXIII*, vol. 11327 S. Owa, ed., International Society for Optics and Photonics (SPIE, 2020), p. 1132706.
17. B. Zhu, S. Zheng, Z. Yu, *et al.*, "L2o-ilt: Learning to optimize inverse lithography techniques," IEEE Transactions on Computer-Aided Design of Integrated Circuits and Systems p. 1 (2023).
18. T. Fuhner and A. Erdmann, "Improved mask and source representations for automatic optimization of lithographic process conditions using a genetic algorithm," in *Optical Microlithography XVIII*, vol. 5754 B. W. Smith, ed., International Society for Optics and Photonics (SPIE, 2005), pp. 415–426.
19. Z. Zhang, S. Li, X. Wang, *et al.*, "Fast heuristic-based source mask optimization for euv lithography using dual edge evolution and partial sampling," Opt. Express **29**(14), 22778–22795 (2021).
20. Z. Zhang, S. Li, X. Wang, *et al.*, "Source mask optimization for extreme-ultraviolet lithography based on thick mask model and social learning particle swarm optimization algorithm," Opt. Express **29**(4), 5448–5465 (2021).
21. A. Poonawala and P. Milanfar, "Mask design for optical microlithography—an inverse imaging problem," IEEE Trans. on Image Process. **16**(3), 774–788 (2007).
22. X. Ma, Z. Wang, X. Chen, *et al.*, "Gradient-based source mask optimization for extreme ultraviolet lithography," IEEE Trans. Comput. Imaging **5**(1), 120–135 (2019).
23. X. Ma and G. R. Arce, "Binary mask optimization for forward lithography based on the boundary layer model in coherent systems," J. Opt. Soc. Am. A **26**(7), 1687–1695 (2009).
24. N. Lafferty, S. Saxena, K. Mizuuchi, *et al.*, "EUV full-chip curvilinear mask options for logic via and metal patterning," in *DTCO and Computational Patterning II*, vol. 12495 R.-H. Kim and N. V. Lafferty, eds., International Society for Optics and Photonics (SPIE, 2023), p. 124950K.
25. K. Hooker, G. Xiao, Y.-P. Tang, *et al.*, "Curvilinear mask solutions for full-chip EUV lithography," in *Novel Patterning Technologies 2022*, vol. 12054 E. M. Panning and J. A. Liddle, eds., International Society for Optics and Photonics (SPIE, 2022), p. 1205407.
26. P. He, J. Liu, H. Gu, *et al.*, "Euv mask model based on modified born series," Opt. Express **31**(17), 27797–27809 (2023).
27. C. M. Lalau-Keraly, S. Bhargava, O. D. Miller, *et al.*, "Adjoint shape optimization applied to electromagnetic design," Opt. Express **21**(18), 21693–21701 (2013).
28. S. Molesky, Z. Lin, A. Y. Piggott, *et al.*, "Inverse design in nanophotonics," Nat. Photonics **12**(11), 659–670 (2018).

29. E. Soubies, T.-A. Pham, and M. Unser, "Efficient inversion of multiple-scattering model for optical diffraction tomography," Opt. Express **25**(18), 21786–21800 (2017).
30. I. M. Mitchell, "The flexible, extensible and efficient toolbox of level set methods," J. Sci. Comput. **35**(2-3), 300–329 (2008).
31. A. Poonawala and P. Milanfar, "A pixel-based regularization approach to inverse lithography," Microelectron. Eng. **84**(12), 2837–2852 (2007).
32. X. Ma and G. R. Arce, "Pixel-based opc optimization based on conjugate gradients," Opt. Express **19**(3), 2165–2180 (2011).
33. Y. Granik, "Fast pixel-based mask optimization for inverse lithography," J. Micro/Nanolithogr., MEMS, MOEMS **5**(4), 043002 (2006).
34. W. Lv, Q. Xia, and S. Liu, "Mask-filtering-based inverse lithography," J. Micro/Nanolithogr., MEMS, MOEMS **12**(4), 043003 (2013).
35. B. Krüger, T. Brenner, and A. Kienle, "Solution of the inhomogeneous maxwell's equations using a born series," Opt. Express **25**(21), 25165–25182 (2017).
36. D. Peng, P. Hu, V. Tolani, *et al.*, "Toward a consistent and accurate approach to modeling projection optics," in *Optical Microlithography XXIII*, vol. 7640 M. V. Dusa and W. Conley, eds., International Society for Optics and Photonics (SPIE, 2010), p. 76402Y.
37. R. A. Lawson and A. P. Robinson, "Chapter 1 - overview of materials and processes for lithography," in *Materials and Processes for Next Generation Lithography*, vol. 11 of *Frontiers of Nanoscience* A. Robinson and R. Lawson, eds. (Elsevier, 2016), pp. 1–90.
38. N. Davydova, J. Finders, J. McNamara, *et al.*, "Fundamental understanding and experimental verification of bright versus dark field imaging," in *Extreme Ultraviolet Lithography 2020*, vol. 11517 P. P. Naulleau, P. A. Gargini, T. Itani, *et al.*, eds., International Society for Optics and Photonics (SPIE, 2020), p. 115170P.
39. V. Philipsen, E. Hendrickx, R. Jonckheere, *et al.*, "Actinic characterization and modeling of the EUV mask stack," in *29th European Mask and Lithography Conference*, vol. 8886 U. F. W. Behringer and W. Maurer, eds., International Society for Optics and Photonics (SPIE, 2013), p. 88860B.
40. A. Erdmann, H. Mesilhy, and P. Evanschitzky, "Attenuated phase shift masks: a wild card resolution enhancement for extreme ultraviolet lithography?" J. Micro/Nanopattern. Mats. Metro. **21**(02), 020901 (2022).
41. R. P. Brent, *Algorithms for minimization without derivatives* (Courier Corporation, 2013).
42. T. Sauer, *Numerical Analysis* (Addison-Wesley Publishing Company, USA, 2011), 2nd ed.
43. B. J. Lin, "Image formation," in *Optical Lithography: Here is Why*, 2 Edition, (SPIE, 2021).
44. A. K.-K. Wong, *Optical imaging in projection microlithography*, vol. 66 (SPIE press, 2005).

Supplemental Document

Optics EXPRESS

Linearized EUV mask optimization based on the adjoint method: supplement

PINXUAN HE,[1] JIAMIN LIU,[1,3] HONGGANG GU,[1] HAO JIANG,[1] AND SHIYUAN LIU[1,2,4,]

[1] *State Key Laboratory of Intelligent Manufacturing Equipment and Technology, Huazhong University of Science and Technology, Wuhan, Hubei 430074, China*
[2] *Optics Valley Laboratory, Wuhan, Hubei 430074, China*
[3] *jiaminliu@hust.edu.cn*
[4] *shyliu@hust.edu.cn*

This supplement published with Optica Publishing Group on 22 February 2024 by The Authors under the terms of the Creative Commons Attribution 4.0 License in the format provided by the authors and unedited. Further distribution of this work must maintain attribution to the author(s) and the published article's title, journal citation, and DOI.

Supplement DOI: https://doi.org/10.6084/m9.figshare.25206890

Parent Article DOI: https://doi.org/10.1364/OE.517783

Linearized EUV mask optimization based on adjoint method: supplemental document

1. DERIVATION OF THE ADJOINT SIMULATION

The derivation in this section focuses on the gradient calculation of the mask model. Given a small perturbation $d\mathbf{E}^{\text{mask}}$, the resulting change dF in the cost function F can be expressed as:

$$dF = \text{Re}\left\{\mathbf{S}^{\text{A}} d\mathbf{E}^{\text{mask}}\right\} \tag{S1}$$

where $\mathbf{S}^{\text{A}}$ is a vector containing the partial derivative of F with respect to $\mathbf{E}^{\text{mask}}$. Details of $\mathbf{S}^{\text{A}}$ can be found in Sec. 2. Then, the equation representing the mask model is rewritten as

$$\mathbf{E}^{\text{mask}} = \mathbf{G}\mathbf{V}(\mathbf{\Theta})\mathbf{E}^{\text{mask}} + \mathbf{G}\mathbf{S} \tag{S2}$$

Next, a perturbation $d\mathbf{V}$ in the scattering potential $\mathbf{V}$ is introduced in Eq. (S2).

$$\mathbf{E}^{\text{mask}} + d\mathbf{E}^{\text{mask}} = \mathbf{G}\left(\mathbf{V} + d\mathbf{V}\right)\left(\mathbf{E}^{\text{mask}} + d\mathbf{E}^{\text{mask}}\right) + \mathbf{G}\mathbf{S} \tag{S3}$$

where $d\mathbf{E}^{\text{mask}}$ is a vector representing the corresponding change of the field. Note that $d\mathbf{V}$ is a diagonal matrix.

$$d\mathbf{V}\mathbf{E}^{\text{mask}} = \hat{\mathbf{E}}^{\text{mask}} d\hat{\mathbf{V}} \tag{S4}$$

where $\hat{\mathbf{E}}^{\text{mask}} = diag(\mathbf{E}^{\text{mask}})$ and $d\hat{\mathbf{V}}$ is a vector containing the main diagonal elements of $d\mathbf{V}$. By combining Eq. (S2) and Eq. (S3) and ignoring the higher-order term, we obtain

$$d\mathbf{E}^{\text{mask}} = \left(\mathbf{G}^{-1} - \mathbf{V}\right)^{-1} \hat{\mathbf{E}}^{\text{mask}} d\hat{\mathbf{V}} \tag{S5}$$

Substituting Eq. (S5) into Eq. (S1), we get

$$dF = \text{Re}\left\{\mathbf{E}^{A} \hat{\mathbf{E}}^{\text{mask}} d\hat{\mathbf{V}}\right\} \tag{S6}$$

where

$$\mathbf{E}^{A} = \mathbf{S}^{\text{A}}\left(\mathbf{G}^{-1} - \mathbf{V}\right)^{-1} \tag{S7}$$

Considering that $\mathbf{G} = \mathbf{G}^{T}$, Eq. (S7) can be rewritten in the form of Eq. (S2).

$$\left(\mathbf{E}^{A}\right)^{T} = \mathbf{G}\mathbf{V}\left(\mathbf{E}^{A}\right)^{T} + \mathbf{G}\left(\mathbf{S}^{\text{A}}\right)^{T} \tag{S8}$$

where T represents the transpose. Eq. (S8) takes $\left(\mathbf{S}^{\text{A}}\right)^{T}$ as the incident field and calculates the diffraction of the EUV mask like Eq. (S2), which is called the adjoint simulation [1, 2]. Then, the chain rule is applied to connect dF and the perturbation in the design variable $d\mathbf{\Theta}$.

$$dF = \text{Re}\left\{\mathbf{E}^{A} \hat{\mathbf{E}}^{\text{mask}} \mathbf{C}_{\text{v}} d\mathbf{\Theta}\right\} \tag{S9}$$

where $\mathbf{C}_{\text{v}}$ is a diagonal matrix representing the partial derivative of $\hat{\mathbf{V}}$ with respect to $\mathbf{\Theta}$. Details of $\mathbf{C}_{\text{v}}$ can be found in Sec. 3. Finally, the gradient of the cost function is

$$\frac{\partial F}{\partial \mathbf{\Theta}} = \text{Re}\left\{\mathbf{E}^{A} \hat{\mathbf{E}}^{\text{mask}} \mathbf{C}_{\text{v}}\right\} \tag{S10}$$

2. DERIVATION OF THE SOURCE OF ADJOINT SIMULATION

In this section, we derive the source of adjoint simulation $\mathbf{S}_A$. The derivation comprises two steps. The first step is to take the derivative of all equations in the lithography model except the EUV mask model. Then, one can combine the resulting equations to get $\mathbf{S}_A$. From the definition of the cost function, we have

$$dF = 2\left(\mathbf{w}^{\mathrm{c}} - \mathbf{w}^{\mathrm{t}}\right) \odot d\mathbf{w}^{\mathrm{c}} \tag{S11}$$

where $\odot$ represents the Hadamard product. Using the resist model, we obtain

$$d\mathbf{w}^{\mathrm{c}} = a\mathbf{w}^{\mathrm{c}} \odot \left(1 - \mathbf{w}^{\mathrm{c}}\right) \odot d\mathbf{I} \tag{S12}$$

Note that the intensity is real number, while the field components are complex numbers. Following the Ref. [3], we have

$$d\mathbf{I} = 2\mathrm{Re}\left\{conj\left(\mathbf{E}_{\mathrm{x}}^{\mathrm{wafer}}\right) \odot d\mathbf{E}_{\mathrm{x}}^{\mathrm{wafer}} + conj\left(\mathbf{E}_{\mathrm{y}}^{\mathrm{wafer}}\right) \odot d\mathbf{E}_{\mathrm{y}}^{\mathrm{wafer}} + conj\left(\mathbf{E}_{\mathrm{z}}^{\mathrm{wafer}}\right) \odot d\mathbf{E}_{\mathrm{z}}^{\mathrm{wafer}}\right\} \tag{S13}$$

The notation $conj$ represents the complex conjugate operator. The derivative of projection model is straightforward.

$$\begin{bmatrix} d\mathbf{E}_{\mathrm{x}}^{\mathrm{wafer}} \\ d\mathbf{E}_{\mathrm{y}}^{\mathrm{wafer}} \\ d\mathbf{E}_{\mathrm{z}}^{\mathrm{wafer}} \end{bmatrix} = \mathbf{H} \begin{bmatrix} d\mathbf{E}_{\mathrm{x}}^{\mathrm{near}} \\ d\mathbf{E}_{\mathrm{y}}^{\mathrm{near}} \\ d\mathbf{E}_{\mathrm{z}}^{\mathrm{near}} \end{bmatrix} \tag{S14}$$

Note that $\mathbf{E}^{\mathrm{near}}$ represents a 2D field distribution. A matrix $\mathbf{C}_{\mathrm{S}}$ is added to represent the slicing operation on the 3D field distribution $\mathbf{E}^{\mathrm{mask}}$.

$$\begin{bmatrix} \mathbf{E}_{\mathrm{x}}^{\mathrm{near}} \\ \mathbf{E}_{\mathrm{y}}^{\mathrm{near}} \\ \mathbf{E}_{\mathrm{z}}^{\mathrm{near}} \end{bmatrix} = \mathbf{C}_{\mathrm{S}} \begin{bmatrix} \mathbf{E}_{\mathrm{x}}^{\mathrm{mask}} \\ \mathbf{E}_{\mathrm{y}}^{\mathrm{mask}} \\ \mathbf{E}_{\mathrm{z}}^{\mathrm{mask}} \end{bmatrix} \tag{S15}$$

Combining all the equations above, we obtain

$$\mathbf{S}_A = \frac{\partial F}{\partial \mathbf{E}^{\mathrm{mask}}} = \begin{bmatrix} \mathbf{E}_{\mathrm{x}}^{\mathrm{wafer}} \\ \mathbf{E}_{\mathrm{y}}^{\mathrm{wafer}} \\ \mathbf{E}_{\mathrm{z}}^{\mathrm{wafer}} \end{bmatrix}^{\dagger} \mathbf{C}_{\mathrm{I}}\mathbf{H}\mathbf{C}_{\mathrm{S}} \tag{S16}$$

where

$$\mathbf{C}_{\mathrm{I}} = \mathbf{I}_{3\times 3} \otimes diag\left\{4a\mathrm{i}\left(\mathbf{w}^{\mathrm{c}} - \mathbf{w}^{\mathrm{t}}\right) \odot \mathbf{w}^{\mathrm{c}} \odot \left(1 - \mathbf{w}^{\mathrm{c}}\right)\right\} \tag{S17}$$

$\otimes$ and $\odot$ represent Kronecker and Hadamard product, respectively. $\dagger$ represents the conjugate transpose. $\mathbf{I}_{3\times 3}$ is a 3×3 identity matrix. The imaginary unit i is introduced by the convolution with the green function [4].

3. DERIVATION OF THE COEFFICIENT MATRIX

In this section, we derive the matrix $\mathbf{C}_{\mathrm{V}}$ representing the partial derivative of $\hat{\mathbf{V}}$ with respect to $\mathbf{\Theta}$. The derivation is similar to that of $\mathbf{S}_A$. Therefore, only the definition of the potential $\hat{\mathbf{V}}$ is presented [5]. The definition of $\hat{\mathbf{V}}$ is

$$\hat{\mathbf{V}} = \left(k_0\mathbf{n}\right)^2 - k_0^2 - i\varepsilon \tag{S18}$$

where k_0 is the vacuum wave vector; $\mathbf{n}$ is the complex refractive index which is defined as

$$\mathbf{n} = n_{bg} + \mathbf{m}_{3\mathrm{D}}\left(n_{abs} - n_{bg}\right) \tag{S19}$$

where n_{bg} is the background refractive index; n_{abs} is the refractive index of absorber. $\mathbf{m}_{3\mathrm{D}}$ is a vector describing the artificial density of absorber in the 3D simulation domain, which is generated by extruding the 2D pattern in $\mathbf{m}$.

$$\mathbf{m}_{3\mathrm{D}} = \mathbf{C}_{\mathrm{D}}\mathbf{m} \tag{S20}$$

where

$$\mathbf{m} = \frac{1 + \cos\left(\mathbf{\Theta}\right)}{2} \tag{S21}$$

$\mathbf{C}_\mathrm{D}$ is a matrix representing the extrusion. After taking the derivative of all equations above, we obtain

$$\mathbf{C}_\mathrm{v} = \frac{\partial \hat{\mathbf{V}}}{\partial \mathbf{\Theta}} = \mathrm{diag}\left\{k_0^2 \left(n_{abs} - n_{bg}\right) \mathbf{n}\right\} \mathbf{C}_\mathrm{D} \mathrm{diag}\left\{\sin\left(\mathbf{\Theta}\right)\right\} \tag{S22}$$

4. AERIAL AND RESIST IMAGES

The aerial and resist images of the logic and BigMac patterns are shown in Fig. (S1) and Fig. (S2), respectively. The figures in the left column are for the original patterns, and those in the right column are for the optimized patterns. The figures in the upper row are aerial images, and those in the lower row are resist images. The aerial images of the optimized patterns exhibit better contrast than those of the original pattens in both examples, which leads to better resist images. The results show that the mask optimizations are necessary and effective.

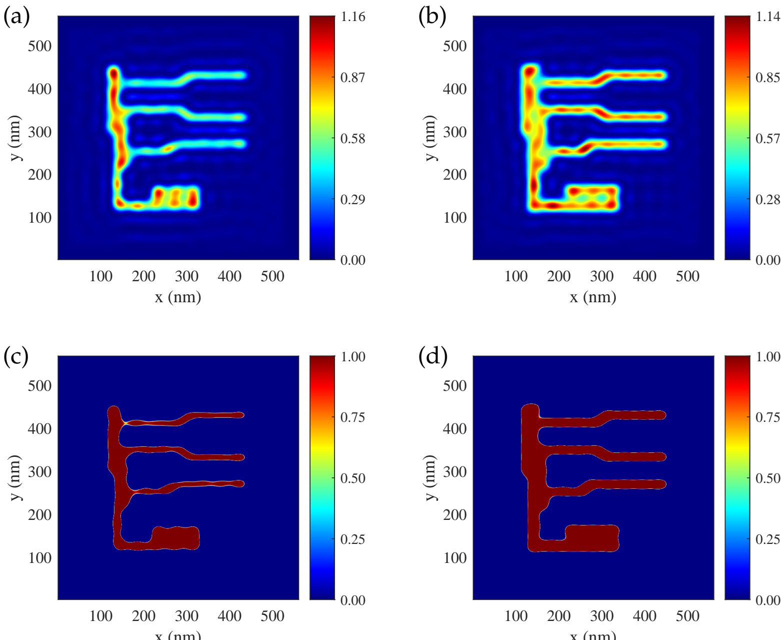

Fig. S1. The aerial and resist images of the logic pattern. The aerial images (a) before and (b) after optimization. The resist images (c) before and (d) after optimization.

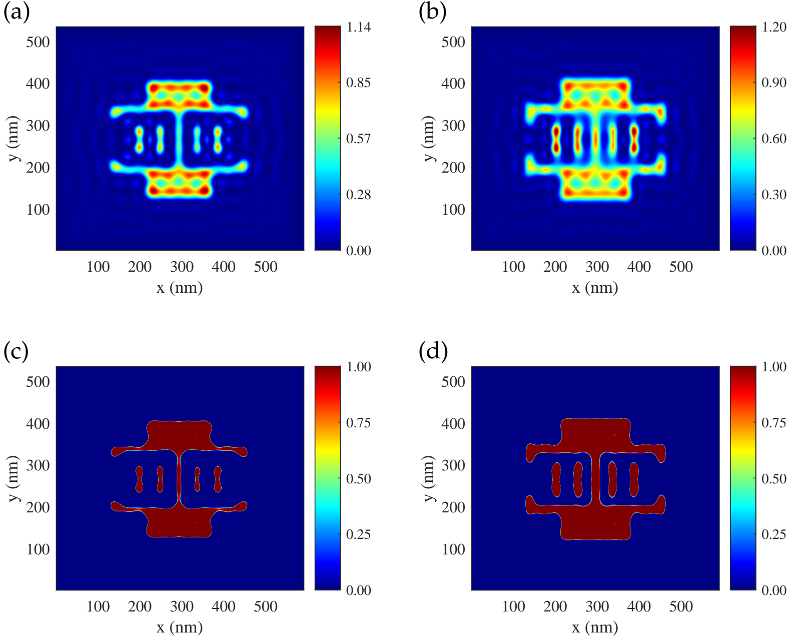

Fig. S2. The aerial and resist images of the BigMaC pattern. The aerial images (a) before and (b) after optimization. The resist images (c) before and (d) after optimization.

REFERENCES

1. C. M. Lalau-Keraly, S. Bhargava, O. D. Miller, and E. Yablonovitch, "Adjoint shape optimization applied to electromagnetic design," Opt. Express **21**, 21693–21701 (2013).
2. N. Georgieva, S. Glavic, M. Bakr, and J. Bandler, "Feasible adjoint sensitivity technique for em design optimization," IEEE Transactions on Microw. Theory Tech. **50**, 2751–2758 (2002).
3. A. Hjørungnes, *Theory of Complex-Valued Matrix Derivatives* (Cambridge University Press, 2011), p. 43–69.
4. M. Lee, H. Hugonnet, and Y. Park, "Inverse problem solver for multiple light scattering using modified born series," Optica **9**, 177–182 (2022).
5. G. Osnabrugge, S. Leedumrongwatthanakun, and I. M. Vellekoop, "A convergent born series for solving the inhomogeneous helmholtz equation in arbitrarily large media," J. Comput. Phys. **322**, 113–124 (2016).